Intermediate temperature embrittlement in a precipitation-hardened high-entropy alloy: The role of heterogeneous strain distribution and environmentally assisted intergranular damage

B.X. Cao [a, b], D.X. Wei [c], X.F. Zhang [d], H.J. Kong [e], Y.L. Zhao [f], J.X. Hou [a], J.H. Luan [a], Z.B. Jiao [g], Y. Liu [h], T. Yang [a, b, *], C.T. Liu [a, b, e, **]

a Department of Materials Science and Engineering, City University of Hong Kong, Hong Kong, China
b Hong Kong Institute for Advanced Study, City University of Hong Kong, Hong Kong, China
c Institute for Materials Research, Tohoku University, 2-1-1 Katahira, Sendai, Miyagi, 980-8577, Japan
d National Engineering Laboratory for Modern Materials Surface Engineering Technology & the Key Lab of Guangdong for Modern Surface Engineering Technology, Institute of New Materials, Guangdong Academy of Science, 510650, Guangzhou, China
e Department of Mechanical Engineering, City University of Hong Kong, Hong Kong, China
f School of Materials Science and Engineering, Harbin Institute of Technology, Shenzhen, China
g Department of Mechanical Engineering, The Hong Kong Polytechnic University, Hong Kong, China
h State Key Laboratory of Powder Metallurgy, Central South University, Changsha, 410083, PR China

Abstract

Severe intergranular embrittlement has been found in a wide range of polycrystalline metallic materials in the intermediate temperature regime, setting severe limits on their engineering applications. In this study, we have systematically investigated the origin of such temperature-dependent premature tensile failure in a precipitation-hardened high-entropy alloy. We highlight the role of heterogeneous strain distribution and environmental attack in facilitating intergranular crack initiation and propagation at intermediate temperatures. The dislocation accumulation has been found in the vicinity of grain boundaries to accommodate thermally activated grain-boundary sliding. Grain boundaries with extensive dislocation pile-ups served as preferential sites for the initiation of voids and associated cracks. The growth and linkage of microcracks lead to the destructive tensile failure. More importantly, environmentally assisted grain-boundary damage plays a vital role in exacerbating the embrittlement. In contrast to the laboratory air atmosphere, tensile testing in an inert argon atmosphere protected the specimens from the environmental damage and helped to recover the tensile ductility at intermediate temperatures. Electron microscopy analyses have uncovered unique deformation substructures, in which both Orowan looping and particle shearing took place. These findings provide a fundamental understanding of the temperature-

dependent deformation behaviors of polycrystalline high-entropy alloys, and this understanding is of a great significance for developing high-performance structural materials for elevated temperature applications.

1. Introduction

The emergence of multi-component high-entropy alloys (HEAs) provides an abundant alloy design space for developing high-performance alloys aiming for advanced engineering applications [[1], [2], [3], [4]]. Introducing nanoscale coherent $L1_2$-type precipitates into the face-centered cubic (FCC) matrix significantly strengthen the alloys without sacrificing the tensile ductility, opening a new era for designing advanced structure materials with both high strength and large ductility [5]. These precipitation-hardened high-entropy alloys (PH-HEAs) have demonstrated many attractive mechanical properties over a wide temperature range. For example, due to the pronounced dislocation cross-slip events, microbanding served as an alternative deformation mechanism in the PH-HEAs, resulting in a stress delocalization and the enhanced work-hardening capabilities at ambient temperature [6]. Moreover, the $L1_2$-strengthened HEA possesses even better tensile properties at cryogenic temperatures due to the dynamic formation of high-density stacking faults and associated microstructural refinement effect, leading to a high tensile strength of 1.7 GPa and a large ductility of 51% at 77 K [7]. Given the similar microstructures to conventional Ni-based superalloys with coherent $L1_2$ particles embedded in the FCC matrix, these $L1_2$-strengthened HEAs preserve an outstanding thermal stability with retarded particle coarsening kinetics [8]. These interesting properties stimulated a series of explorations of applying PH-HEAs towards elevated temperature environments [[9], [10], [11]]. It should be noted that most of the PH-HEAs designed for cryogenic and ambient temperature applications possess a small volume fraction of the $L1_2$ phase with an inadequate heat resistance. For example, the volume fraction of the $L1_2$ phase is only ~20% among the $(NiCoCr)_{94}Al_3Ti_3$ (at.%) alloy, which vanished as the temperature increased above 900 °C [8]. Since a high $L1_2$ volume fraction is favorable for providing a sufficient deformation resistance at elevated temperatures, efforts have been devoted to stabilizing the $L1_2$ particles above 1100 °C through balanced alloying additions [12]. The newly developed PH-HEA has demonstrated an outstanding high-temperature strength, which is even superior to commercial Ni-based superalloy Waspaloy [13]. These encouraging results justify the motivation to pursue high-temperature applications within $L1_2$-strengthened high-entropy alloy systems.

Particular attention should be given to the grain-boundary regions in evaluating the engineering potential of polycrystalline PH-HEAs [14]. On the one hand, grain boundaries act as potent barriers against dislocation slip transmission. Therefore, the grain refinement can effectively elevate the strength of polycrystalline alloys, which is also commonly known as the Hall-Petch strengthening [15]. On the other hand, grain boundaries also serve as weak points and act as preferential crack nucleation sites and

loci for grain boundary sliding, especially at elevated temperatures [16,17]. Therefore, the intergranular fracture has been frequently observed in many engineering materials due to the preferential damage accumulation localized at the grain-boundary regions [18]. Moreover, distinctly different compositional and structural interfacial states from those at grain interiors can also be stabilized at grain boundaries, whose existence profoundly influences the thermo-mechanical properties, including grain-boundary mobility, grain-boundary cohesive strength, and tensile ductility [12,19]. For example, chemical segregation at grain boundaries has been observed in the CoCrFeMnNi HEA, which is responsible for the preferential intergranular crack initiation and associated embrittlement [20]. Through triggering the multi-element co-segregation at grain boundaries, Yang et al. [21] induced a nanoscale disordered grain boundary layer (FCC structured) in an $L1_2$-based high-entropy intermetallic alloy. Instead of causing intergranular cohesion loss, such grain-boundary disordered layer allows an easier dislocation slip transfer between neighboring grains, leading to an extraordinary strength-ductility synergy [21]. Therefore, the role of grain boundaries on plastic deformation and their correlations with tensile properties are worthy of in-depth investigations.

In our recent investigations, we observed the formation of the $L2_1$-type Heusler phase at grain boundaries in the Ni–30Co–13Fe–15Cr–6Al–6Ti-0.1B (at.%) PH-HEA [22]. The brittle Heusler phase acts as a preferential site for crack initiation and propagation upon plastic deformation, causing a severe embrittlement along grain boundaries. Through a novel duplex-aging heat treatment, we have demonstrated that the precipitation of the intergranular $L1_2$ particles helps to pin the grain boundaries and retard their migrations. By this way, the formation of Heusler phase can be effectively suppressed, contributing to the brittle-to-ductile transition and the recovered tensile ductility at 700 °C [22]. However, as the deformation temperature increased to 800 °C, polycrystalline PH-HEA with the duplex-aging heat treatment still suffered from severe brittleness with massive intergranular facets on the fracture surface [23]. By tailoring grain-boundary characters and structures via thermo-mechanical treatments, we introduced the heterogeneous columnar-grained structures to reduce the fraction of high-angle random grain boundaries (HARGBs) and disrupt the connectivity of HARGBs. The crack propagation path can be blocked by such a heterogeneous grain structure, leading to a distinct intergranular-to-transgranular transition and associated regained tensile ductility (~18% plastic strain) at 800 °C [23]. Though this structure can effectively inhibit grain-boundary embrittlement, it should be noted that the heterogeneous columnar-grained structure might be thermodynamically unstable, which tends to transform into the polycrystalline structure with a prolonged annealing [24].

Since most engineering materials are still employed in the polycrystalline form, and therefore, it is of a vital importance to understand the intrinsic origins for the dramatic ductility loss at intermediate temperatures [25]. Herein, we have systematically investigated the tensile deformation of the PH-HEA at various testing conditions, including both ambient and elevated temperatures, oxidative laboratory air, and protective argon atmosphere. These findings not only provide a fundamental insight

into the intrinsic mechanisms that govern the tensile embrittlement, but also promote the engineering applications of PH-HEAs towards elevated temperature environments.

2. Experiment

2.1. Materials preparation

Alloys with a nominal composition of Ni–30Co–13Fe–15Cr–6Al–6Ti-0.1B (at.%) were prepared by arc melting high-purity raw metals (>99.9 wt%) in a Ti-gettered high-purity Ar atmosphere. The ingots were flipped and remelted at least five times before drop cast into a water-cooled copper mold. These cast samples were homogenized at 1165 °C for 2 h, and then cold-rolled with ~65% reduction in thickness, followed by recrystallization at 1165 °C for 2 mins. The fully recrystallized HEAs were first isothermally aged at 1000 °C for 4 h, followed by a secondary aging treatment at 800 °C for 16 h for the growth of $L1_2$ particles. The adoption of the duplex-aging treatment can stabilize grain boundaries and suppress intergranular Heusler phase formation [22]. The as-aged PH-HEA exhibited a clean "FCC + $L1_2$" dual-phase microstructure without the formation of other brittle intermetallic phases.

Thermal barrier coating was deposited via a coating machine (AS-700, ProChina Limited, Beijing, China). The surface of the as-aged PH-HEAs were mechanically polished before coating. The CoCrAlY alloy was used as the target upon deposition, which contains a nominal composition of 25–30 Cr, 7–10 Al, 1–1.5 Y, and the balanced Co (wt.%). The bias voltage and arc current during deposition has been chosen as −100 V and 110 A with a 0.5 Pa working pressure. The duty cycle was maintained as 70%. The total deposition time was 4 h, which resulted in a coating thickness of ~50 μm. The detailed deposition method has been described in a previous work [26].

2.2. Materials characterizations

Microstructural characterizations were carried out via scanning electron microscopy (SEM, Quanta 450), transmission electron microscopy (TEM, JEOL 2100F), and electron back-scattered diffraction (EBSD, EDAX). For SEM observations, the samples were first mechanically grounded by SiC paper, followed by electro-polishing using an electrolyte of 20 vol% nitric acid and 80 vol% ethanol at a direct voltage of 20 V at -40 °C. For TEM analyses, specimens were first grounded by using SiC paper to a thickness of 50 μm and then punched into discs with a diameter of 3 mm. The discs were mechanically dimpled and further thinned by ion-milling to a thickness of electron transparency via a precision ion polishing system (PIPS, Gatan 695). A final cleaning step of 2 keV milling at 2° was applied to avoid potential ion damages.

For the plastically deformed specimens, the EBSD technique was applied to evaluate the plastic strain distribution through misorientation analyses. EBSD data were acquired from the electro-polished specimens. The GND density is calculated to evaluate the local lattice curvature, which can be derived as [27]:(1)$\rho GND=\dfrac{2\theta}{\mu b}$where θ is the misorientation angle, μ is the length of the step size used in the EBSD mapping, and b is the magnitude of the Burgers vector.

To provide insight into the elemental partitioning behavior of the nano-sized $L1_2$ precipitates, we employed atom probe tomography (APT, CAMECA LEAP 5000 XR) for compositional analyses. The APT nanotips were prepared by lift-out

procedures and then annular-milled using a focused-ion-beam/scanning electron microscope (FIB/SEM, FEI, Scios). The APT test was carried out at 70 K in voltage mode with a pulse frequency of 200 kHz, a detection rate of 0.2%, and a pulse fraction of 20%.

2.3. Mechanical tests

Flat dog-bone-shaped tensile specimens with a gauge length of 12.5 mm were prepared by electrical discharge machining. The surfaces of the tensile specimen were carefully grounded by 2500 grit SiC paper before the tensile test to remove possible surface microcracks. Uniaxial tensile tests were conducted in the laboratory air at various temperatures (25, 300, 600, 700, 750, 775, 900, and 950 °C) with a constant strain rate of 1×10^{-3} s^{-1}. Two specimens have been prepared for each tensile testing condition. Three thermal couples were used to monitor the temperature inside the furnace to ensure a temperature fluctuation within ±5 °C during high-temperature tensile deformation. To avoid the environmental attack upon tensile deformation in an oxidizing environment, tensile tests were also conducted in an inert argon atmosphere at 775 °C for comparison. A vacuum condition of 5×10^{-4} Pa was first reached in the testing chamber before backfilling with high-purity argon for protection.

3. Results

3.1. Structure of the L1$_2$-strengthened high-entropy alloy

Representative microstructure of the investigated PH-HEA after a duplex-aging heat treatment at the grain boundary triple junction (where three grain boundaries meet each other in the polycrystalline PH-HEA) was shown in Fig. 1(a). The formation of dense L1$_2$ precipitates is clearly visible throughout the materials, both at the grain interiors and in the vicinity of grain boundaries. Figure 1(b) is the dark-field TEM micrograph, showing the formation of high-density L1$_2$ precipitates with a bimodal size distribution. To highlight the interfacial character between the matrix phase and the L1$_2$ precipitates, a representative high-resolution TEM micrograph was shown in Fig. 1(c), demonstrating the coherent interfacial relationship between the matrix and the precipitates. The Fast Fourier Transforms (FFTs) taken from the L1$_2$ particles and the FCC matrix have been shown in the insets in Fig. 1(c). Superlattice spots in the FFT taken from the particles indicated the ordered nature of the L1$_2$ structure. Figure 1(d) demonstrates the reconstructed APT nanotip with distinctly different chemical compositions between the particles and the matrix phase. Ni, Al, and Ti elements were recognized as potent L1$_2$-stabilizing elements by strongly partitioning to the precipitates. In contrast, Co, Fe, and Cr acted as the L1$_2$-destabilizing elements and were depleted from the particles.
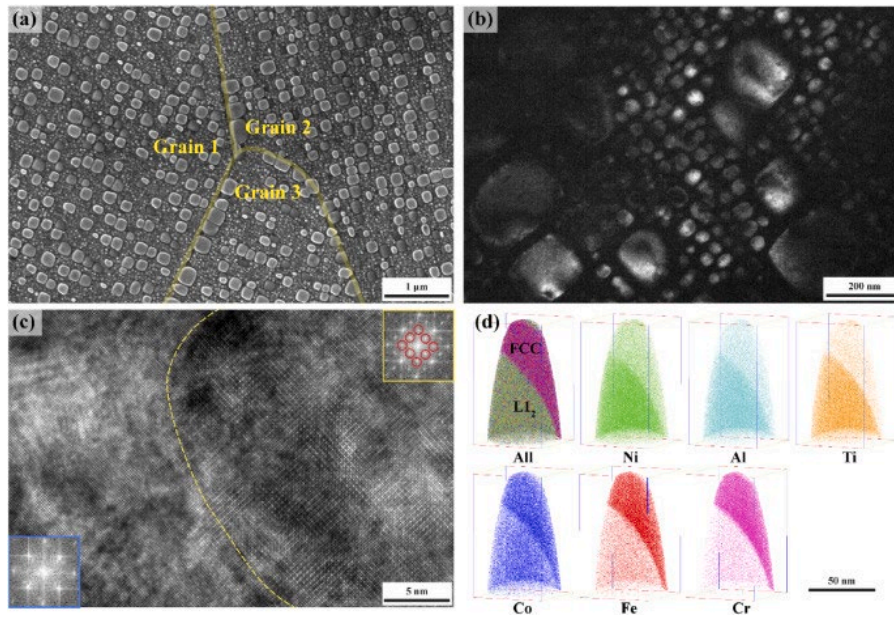
Fig. 1. (a) SEM micrograph of the grain boundary triple junction in the duplex-aged PH-HEA. Grain boundaries are highlighted by yellow lines. (b) Representative dark-field TEM micrograph of the ordered $L1_2$ precipitates with a bimodal size distribution. (c) High-resolution TEM image showing coherent matrix-precipitation interface (highlighted by yellow curves). Corresponding FFTs taken from the $L1_2$ particles and the FCC matrix have been displayed in the insets. (d) Nanoscale elemental partitioning behaviors as revealed by atom probe analyses. Ni, Al, and Ti elements were strongly partitioned to the precipitates, whereas Co, Fe, and Cr were depleted from the precipitates.

3.2. Temperature-dependent tensile ductility

Uniaxial tensile tests were performed at various temperatures ranging from 25 to 950 °C in air. Representative tensile stress-strain curves are shown in Fig. 2(a). Three temperature regimes with distinctively different tensile ductility were discovered. First, an outstanding strength-ductility combination has been achieved at temperatures below 600 °C. For example, the PH-HEA demonstrated a tensile strength over 1.3 GPa and a ductility up to 30% at ambient temperature. According to our previous investigations, such superb strain-hardening capability is originated from the dynamic formation of dense stacking faults and associated microstructural refinement upon plastic deformation [7]. Tensile deformation at 300 and 600 °C also exhibited decent work-hardening capacities with failure elongations over 20%. The serrated stress-strain curves at 300 and 600 °C can be attributed to the Portevin–Le Chatelier effects [28]. Such serrated plastic flow arises from the interactions between the diffusing solute atoms and the mobile dislocations that are temporarily impeded [29]. However, a sudden dip in the tensile ductility was found as the deformation temperature increased above 700 °C. The tensile ductility reached the minimum with a fracture elongation of $3.8 \pm 0.3\%$ at 775 °C. Beyond this ductility minimum regime, the tensile ductility started to regain at elevated temperatures, recovering to $7.4 \pm 1.1\%$ at 900 °C and $18.7 \pm 0.7\%$ at 950 °C, respectively. Tensile strength and ductility values at various

temperatures have been summarized in Table 1. The temperature-dependent tensile ductility was shown in Fig. 2(b), highlighting the ductility minimum regime in the temperature range roughly from 700 to 775 °C. Fracture surface analyses uncovered a distinct ductile-to-brittle fracture mode transition with the increased deformation temperatures (see Fig. 2(c)). Ductile fractures were evidenced by the dimpled transgranular fracture surfaces after strained to failure at 25 and 600 °C. Localized necking can also be clearly seen from the fracture surface of the specimens after the tensile failure at ambient temperature. However, the fracture surface was dominated by the intergranular failure at the temperatures within the ductility minimum regime. Apart from the smooth grain boundary facets, secondary intergranular cracking can also be observed on the fracture surface. Noticeably, a region showing the brittle intergranular failure was surrounded by the dimpled transgranular fracture surfaces after tensile failure at 775 °C (highlighted in Fig. 2(c)). Therefore, the propagated secondary cracks penetrated into the PH-HEAs preferentially along the intergranular paths, leaving behind uncracked ligaments. The left ligaments eventually failed in a ductile manner when local stress exceeds the tensile strength of the PH-HEA, resulting in the mixed intergranular and transgranular fracture surface. As the deformation temperature further increased to 900 and 950 °C, the fracture surfaces consisted of decohesive intergranular facets and fractured in a completely intergranular manner. Intergranular microcracks shown in the representative post-fracture micrograph were distributed preferentially along the vertical direction (Fig. 3), which is roughly perpendicular to the external loading direction. The formation of intergranular microcracks reduced the tensile stress with the proceeding of tensile loading, resulting in the strain softening, as can be seen from the stress-strain curves at elevated temperatures in Fig. 2(a). In short, dimpled transgranular fracture transformed into brittle intergranular fracture when tensioned in the laboratory air with the increased deformation temperatures.
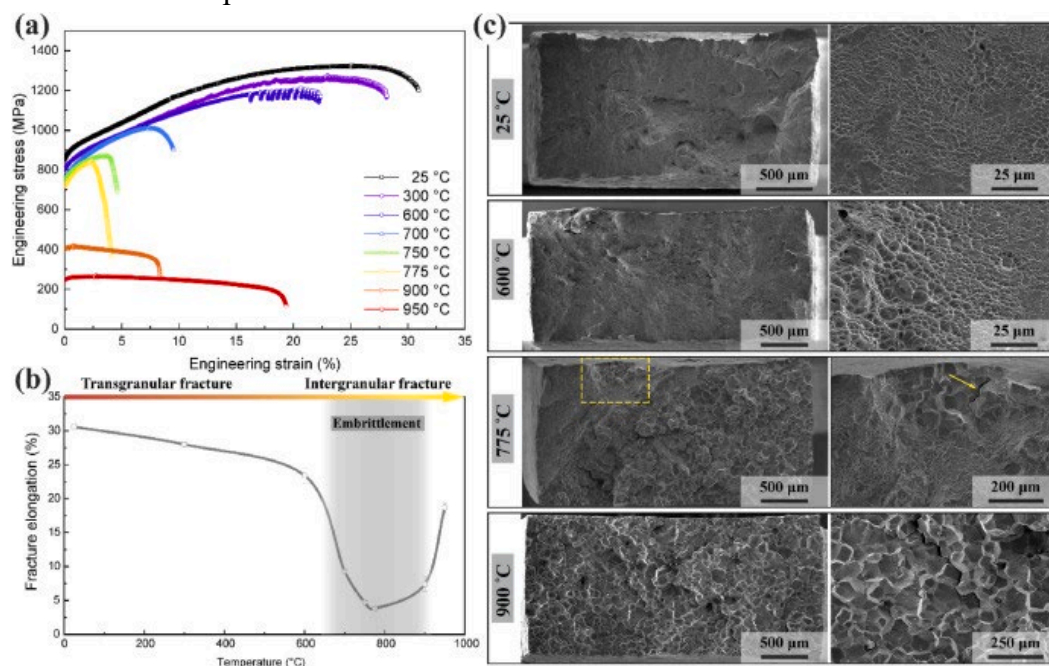
Fig. 2. (a) Representative stress-strain tensile curves at various deformation temperatures (in the laboratory air). (b) Fractured elongation values are plotted as a function of the deformation temperature. Severe embrittlement was found in the intermediate temperature regime. (c) SEM fractography of the PH-HEA specimens at different testing temperatures. Distinct fracture mode transition from a dimpled transgranular fracture to the intergranular fracture was identified as the deformation temperature increased from 25 to 900 °C.
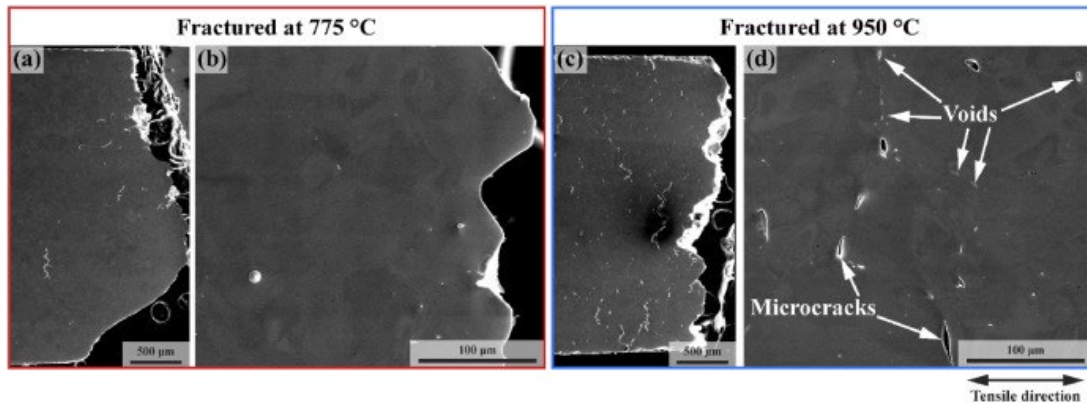

Fig. 3. Representative morphology of the specimens strained to failure at 775 and 950 °C in the laboratory air. (a–b) Few secondary intergranular microcracks appeared in the localized regions for the specimens fractured at 775 °C. (c–d) Extensive intergranular microcracks developed at grain boundaries in the PH-HEA fractured at 950 °C. Tensile voids nucleated along grain boundaries. The coalescence of these voids subsequently resulted in the intergranular microcracks.

3.3. Environment-dependent tensile ductility

To unveil the origins of the severe embrittlement we encountered during tensile deformation in the laboratory air at the intermediate temperatures, we utilized two alternative approaches to protect the PH-HEAs from the environmental damage during high-temperature tensile deformation and to elucidate their intrinsic mechanical responses. First, thermal barrier coatings have been deposited on PH-HEA substrate for protection purposes [30]. The CoCrAlY coating has been commonly applied to the hot-section components in gas turbine engines, aiming to improve components' heat resistance and durability [31]. The coatings are expected to protect the PH-HEA substrate from possible environmental attacks during tensile deformation at elevated temperatures [32]. Second, the high-temperature tensile tests were carried out in a protective argon atmosphere instead of exposure in the laboratory air. As shown in Fig. 4, in contrast to the rapid failure upon tensioned in the laboratory air, both coating deposition and protective tensile atmosphere help to recover the tensile ductility from $3.8 \pm 0.3\%$ to $7.4 \pm 1.0\%$ and $15.0 \pm 0.2\%$, respectively. The effects of the coating deposition and testing environment on tensile properties have been summarized in Table 1. It suggests that the rapid tensile ductility drop is strongly correlated with the environmental interactions. The yield strength and work-hardening

behaviors were not significantly altered by coating deposition or exposing in the inert atmosphere, suggesting that deformation mechanisms were not affected, except for the early crack initiation and propagation as well as associated tensile embrittlement when exposed in an oxidizing environment upon tensile loading.
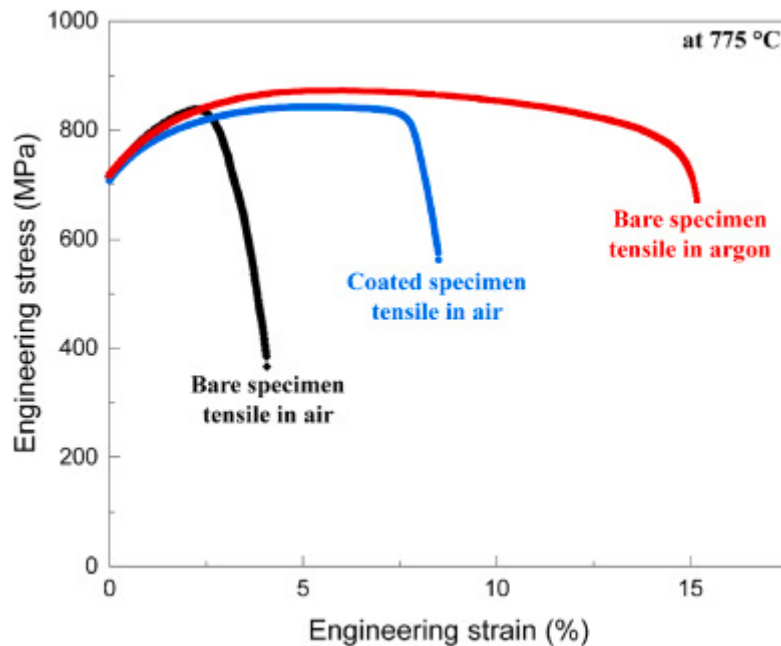

Fig. 4. Representative stress-strain tensile curves at 775 °C with different surface treatments and testing environments. Both thermal barrier coating and protective testing atmosphere help to recover the tensile ductility. The stress-strain curve of bare PH-HEA tensioned in the laboratory air is also shown here for a direct comparison.

4. Discussions

4.1. Origin for the transgranular-intergranular fracture mode transition and the temperature-dependent tensile ductility evolutions

The EBSD technique was applied to study the plastically deformed PH-HEAs to unveil the origins of the transgranular-to-intergranular transition. We chose two representative temperatures, that is, 775 and 950 °C for detailed studies, in which both the PH-HEA specimens exhibited an intergranular fracture. At 775 °C, the specimens encountered severe embrittlement and fractured rapidly at a plastic strain of ~4%. However, it is interesting to note that the tensile ductility recovered as the deformation temperature increased to 950 °C and eventually fractured at a strain of ~19%. For comparison purposes, an additional uniaxial tensile test was interrupted at a strain of ~4% at 950 °C for EBSD analyses. To quantitatively examine the extent of local plastic deformation, geometrically necessary dislocation (GND) density was calculated [27]. Figure 5 illustrates the GND density distribution maps after the deformation of the bare specimens at 775 and 950 °C in air. As evident in Fig. 5(a), the accumulation of dislocations in the vicinity of grain boundaries has been found after strained to failure at 775 °C. In addition, localized plastic flow also developed at grain boundary triple junctions and extended into grain interiors in parallel to one specific grain boundary

that connected to the grain boundary triple junction (illustrated by white arrows in Fig. 5). The GND distribution for the specimen deformed at 950 °C with an identical strain also showed stress concentration along grain boundaries and the extension from grain boundary triple junctions into grain interiors (Fig. 5(b)). However, as compared to the specimens deformed at 775 °C, the intensity of the stress localization in the vicinity of grain boundaries appeared to be less severe at 950 °C under the similar strain magnitude. Apart from the preferential dislocation activities in the vicinity of grain boundaries, dislocation substructures also developed at grain interiors (indicated by the yellow arrow in Fig. 5(b)) and rearranged into subgrain boundaries at 950 °C (Fig. 5(c)). The GNDs accumulated at these subgrain boundaries with further straining, reaching as high as $2 \times 10^{14} \text{ m}^{-2}$. The rearrangement of dislocations into subgrain boundaries with lower-energy dislocation substructure tends to decrease the resistance towards dislocation motion [33]. The histogram in Fig. 5(d) showed the GNDs generated after plastic straining at 775 and 950 °C. Curves for the GND distributions after deformation at 775 and 950 °C with the strain of ~4% were similar with peaks located near $5 \times 10^{13} \text{ m}^{-2}$ for both temperatures. Further straining at 950 °C led to the higher frequency at higher GND density regimes (Fig. 5(d)), which is associated with the continuous GND accumulations to accommodate the local lattice curvature imposed by the external strain.
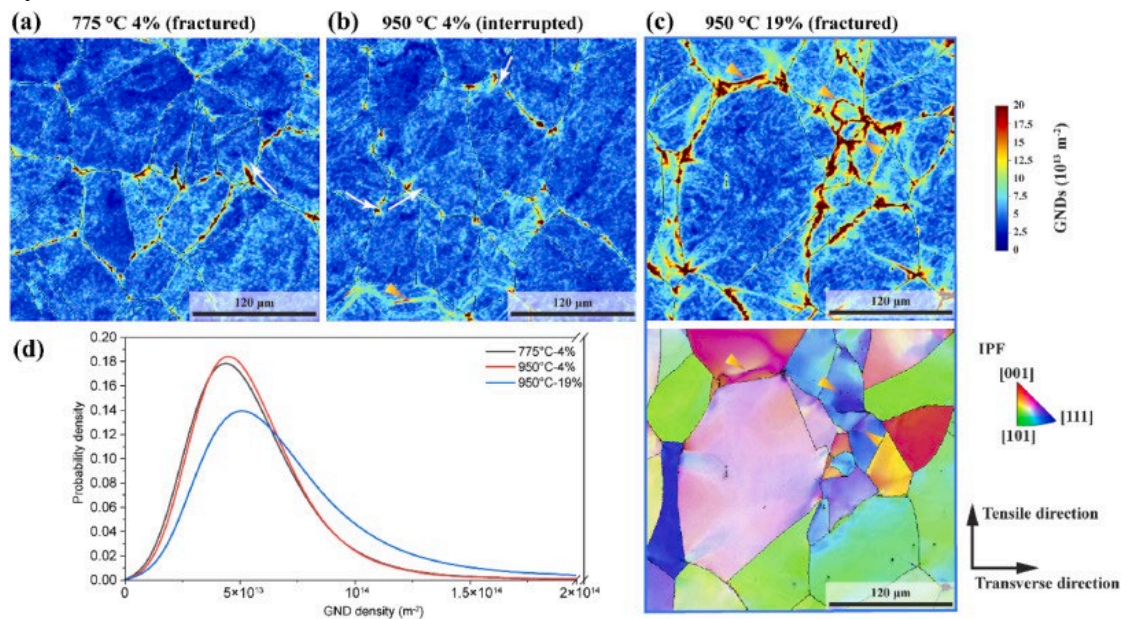

Fig. 5. Geometrically necessary dislocation density maps of the deformed bare PH-HEAs in air: (a) strained for 4% at 775 °C; (b) strained for 4% at 950 °C; (c) strained for 19% at 950 °C. Corresponding inverse pole figure superimposed on the band contrast map of the PH-HEA strained for 19% at 950 °C has also been shown in (c). (d) The probability density function of GNDs.

As described above, smooth intergranular facets were observed on the fracture surface after tensile failure at temperatures above 700 °C, whereas ductile dimples dominate the transgranular fracture surface in a lower temperature regime. Based on these findings, it is safe for us to conclude that both the local stress concentration in the

vicinity of grain boundaries and environmental grain-boundary attacks contributed to the transgranular-to-intergranular fracture mode transition.

First, grain boundary sliding is believed to be thermally activated at elevated temperatures, which can be accommodated by preferential dislocation activities in the vicinity of grain boundaries [34,35]. This process leads to dislocation pile-ups and accumulated local strain at grain boundary regions, which is consistent with the higher GND density along grain boundaries as found in the present investigation (Fig. 5). It should be noted that these grain-boundary regions with higher dislocation density served as the preferential sites for crack initiation [36,37]. Therefore, the formation of numerous intergranular voids at grain boundaries (see Fig. 3) is a result of preferential damage accumulation at grain boundaries. These voids tend to coalesce and interlink into microcracks along grain boundaries with the proceeding of plastic strain, causing a destructive tensile failure. Second, environmental damage also plays a vital role in facilitating the intergranular damage when tensioned in an aggressive atmosphere [38]. To this end, the intrinsic mechanical performance has been well demonstrated by conducting the tensile test in a protective testing atmosphere (Ar) to shield the PH-HEAs from the environmental attack (Fig. 4), in which the tensile ductility recovered from $3.8 \pm 0.3\%$ in the oxidizing atmosphere to $15.0 \pm 0.2\%$ in a protective Ar atmosphere. Previous studies indicated that such embrittlement is mainly associated with the stress-assisted oxygen diffusion ahead of the crack tip [39,40]. The high-energy grain boundaries often served as the fast diffusion paths for damaging species, especially for oxygen penetration along high-angle random grain boundaries at elevated temperatures [41]. The rapidly penetrated oxygen atoms lead to a local grain-boundary cohesion loss ahead of the intergranular crack tips, which allows the crack tip to advance and the embrittling species inwards [42]. The repeated processes lead to a dynamic grain-boundary decohesion, and therefore, the tensile specimens fractured in an intergranular mode.

In strong contrast with the rapid failure in the intermediate temperature regime, the tensile ductility started to recover at temperatures above 775 °C (see Fig. 2(b)). The rapid fracture within the ductility minimum temperature regime can be ascribed to the high crack propagation rate. First, due to the anomalous yield behavior of the $L1_2$ strengtheners at intermediate temperatures [43] and the onset of precipitation dissolution at elevated temperatures (above ~800 °C), PH-HEA retained most of its strength at 775 °C (a yield strength of 708 ± 8 MPa). However, the yield strength of PH-HEA was substantially compromised at higher temperatures, e.g., 416 ± 21 MPa at 900 °C and 249 ± 3 MPa at 950 °C. Therefore, the stress intensity factor at 775 °C is greater than that at 900 and 950 °C; this leads to an accelerated crack propagation at 775 °C. This argument is supported by an oxygen-diffusion-based analytical model proposed by Bika et al. [44], which indicated that the crack propagation rate increased with the increased applied stress at the crack tip. Second, preferential oxygen penetration along grain boundaries can also be assisted by the local strain field [45]. Previous studies indicated that the plastic strain can accelerate damaging species penetration and assist the corrosion of stainless steels [46]. Also, preferential oxygen damage along slip bands with intense plastic deformation has been observed upon

fatigue loading at 725 °C [42]. Grain boundaries with an accumulated plastic strain either provide stored strain energy or act as short-circuit diffusion paths (i.e., dislocations), facilitating the oxygen penetration along intergranular paths [42]. The severe stress concentration at grain boundaries combined with the environmental damage help to initiate intergranular cracks. Once initiated, aided by the high stress intensity factor and the stress-accelerated intergranular oxygen penetration, the intergranular crack propagates rapidly at 775 °C, leading to a rapid tensile failure. In contrast, crack propagation is partially retarded due to the compromised strength at elevated temperatures (e.g., 900 and 950 °C). Moreover, we noticed that secondary intergranular microcracks only appeared in certain localized regions for the specimens fractured at 775 °C and most of grain boundaries remained undamaged (Fig. 3(b)). In contrast, the PH-HEAs tensioned at 950 °C appeared to be more damage tolerant since numerous voids and secondary microcracks have already been initiated (Fig. 3(d)), whereas these microcracks were not interlinked with each other even at a plastic strain of ~19% at this temperature. It should be noted that the tensile failure at temperatures above the intermediate temperature regime should still be ascribed to the concentrated plastic strain and environmental attacks along grain boundaries, the slower crack propagation rate provides more time for the plastic deformation, resulting in the recovered tensile ductility.

4.2. Ductility recovery by coating deposition and protective tensile atmosphere within the intermediate temperature regime

Applying coating partially recovered the tensile ductility to 7.4 ± 1.0% at 775 °C in the oxidizing atmosphere. As pointed out by yellow arrows in Fig. 6(a), the fractured specimens showed multiple secondary cracks on the deposited CoCrAlY coatings. The cross-sectional morphology was revealed after grinding and electro-polishing for detailed failure analyses at the substrate/coating interfaces. The thickness of the CoCrAlY coatings is approximately 50 μm (Fig. 6(b)). A layer with high local misorientation values has been found at the substrate/coating interfaces, suggesting the accumulation of GNDs at the interfaces upon the plastic deformation. Such localized strain at the interface indicated that the plastic deformation between the substrate and the coating is not compatible with each other. Moreover, the presence of multiple secondary cracks on the deposited coatings suggests that the coatings are intrinsically brittle, which cannot deform coordinately with the substrate upon tension [47,48]. Previous studies revealed that the strain on the coatings distributed heterogeneously at an early stage of deformation, which quickly evolved into cracks that initiate from the coating surface and extend through its thickness into the subtract in less than 2% strain [47,48]. Once the deposited coatings failed, it would expose the inner substrate to the oxidizing environment, resulting in a rapid penetration of oxygen along intergranular paths. In addition, Kernel Average Misorientation (KAM) maps also revealed severe stress concentrations along grain boundaries (Fig. 6(d)). As a result, intergranular microcracks initiated and propagated quickly after protection failure, leading to a premature tensile failure. Therefore, the tensile ductility can only be marginally recovered via thermal barrier coating.
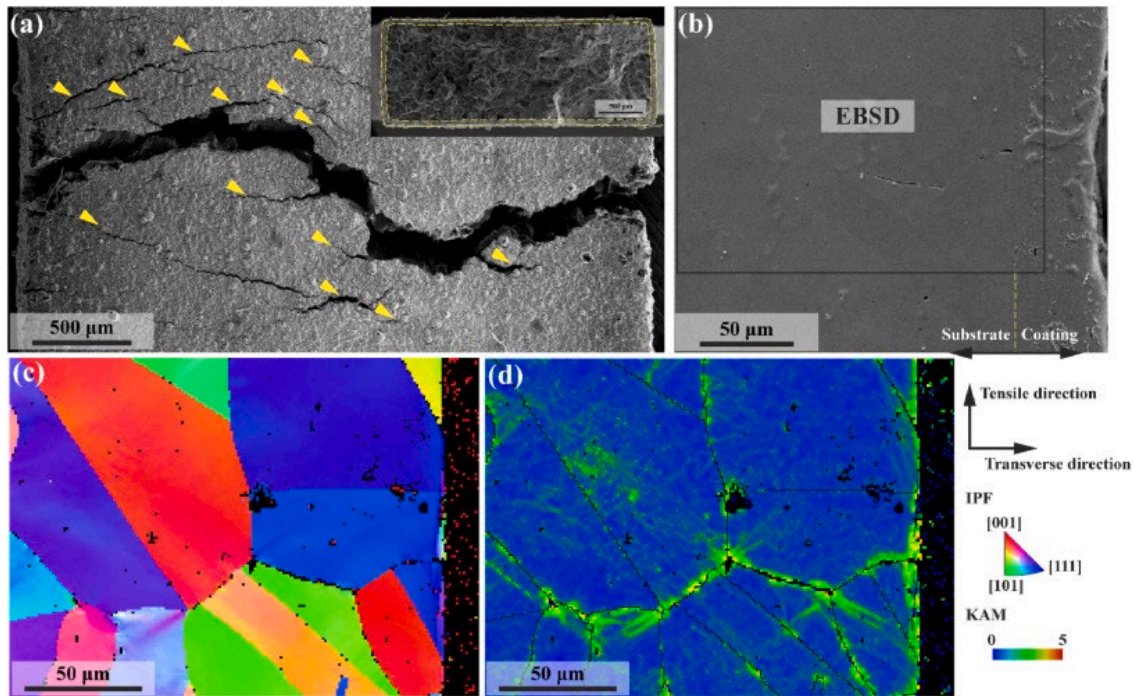
Fig. 6. (a) Oxidized surface morphology of the CoCrAlY coated PH-HEAs strained to failure in the laboratory air at 775 °C, showing multiple secondary cracks generated on the coatings. (b) Profile of the PH-HEA substrate with thermal barrier coatings. (c–d) Inverse pole figure (IPF) map and KAM map showing severe stress concentration at grain boundaries. The localized strain also developed at the interface between the substrate and the coatings. The coating areas were not properly indexed due to the low confidence index values.

Substantial ductility recovery has been observed upon conducting the tensile test at 775 °C in a protective Ar atmosphere (Fig. 4). To reveal the underlying intrinsic mechanical response during the tensile deformation, plastically deformed PH-HEAs (strained for 2% and 15%) were analyzed using the EBSD technique. Corresponding KAM maps have been illustrated in Figs. 7(a-b). It clearly shows that GNDs generated at grain boundary triple junctions and extended into grain interiors due to the thermally activated grain boundary sliding at an early deformation stage. As the tensile strain increased to ∼15%, in addition to the plastic flow at grain boundaries, dislocation activities also generated at grain interiors and contributed to the sustained plastic strain, whereas the specimens tensioned in the laboratory air fractured at ∼4% strain at this temperature, in which deformation still primarily concentrated at grain boundaries without pronounced dislocation activities at grain interiors. Fractographical investigations revealed a mixed intergranular-transgranular fracture morphology in the protective atmosphere at 775 °C (Figs. 7(c-e)). In contrast with the featureless intergranular facets after tensile failure in the laboratory air at the same magnification ratio, well-defined dimples were found on the intergranular facets after tensile failure in a protective atmosphere. The formation of dimpled intergranular facets results from the preferential nucleation, growth, and coalescence of voids along grain boundaries with regard to that at grain interiors [49]. The grain boundary dimpled fracture has also

been previously reported in precipitation-hardened alloys with soft precipitation-free zones adjacent to grain boundaries [49]. The precipitation-free zones cause a strain localization at grain boundary regions, leading to the preferential microvoid initiation and growth at grain boundaries and the resultant dimpled intergranular fracture surfaces [50]. However, we did not observe the formation of precipitation-free zones along grain boundaries in the current PH-HEAs since $L1_2$ precipitates distributed uniformly in the grain interiors as well as grain boundary regions (Fig. 1(a)). Alternatively, thermally activated grain boundary sliding is accommodated by preferential dislocation activities at grain boundaries, leading to a localized strain in the vicinity of the grain boundaries. Such strain concentration at grain boundaries leads to the ductile grain boundary fracture with dimples on the intergranular facets. This demonstrates the intrinsic ductile nature of the grain-boundary region within intermediate temperature regime when the external oxidation damages were avoided.
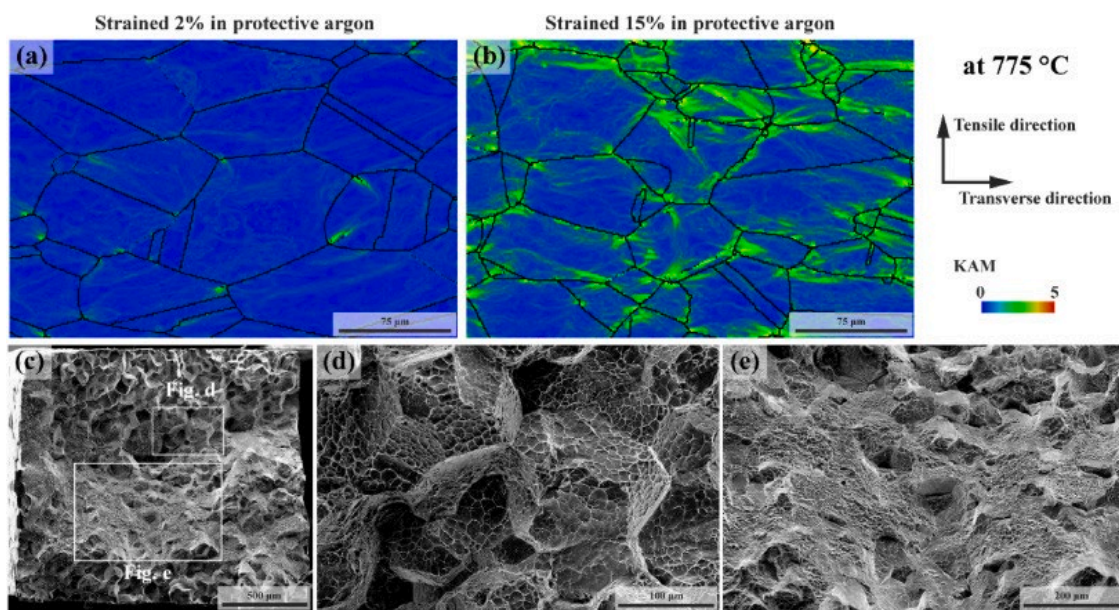

Fig. 7. KAM maps of the bare PH-HEAs tensioned in an inert argon atmosphere at 775 °C with a plastic strain of (a) 2% and (b) 15%. (c–e) The fracture surface of the PH-HEAs, showing mixed fracture mode that consists of both dimpled intergranular surface and dimpled transgranular surface.

4.3. Deformation mechanisms at 775 °C in a protective tensile atmosphere

The deformation substructures after tensile tested at 775 °C in the inert argon atmosphere are presented in Fig. 8. It should be noted that, before the tensile test, the cold-rolled specimens were recrystallized at 1150 °C and followed by duplex aging treatments. These heat treatments are believed to substantially reduce the stored dislocation density. Therefore, it is expected that the observed dislocations were generated upon the tensile deformation at 775 °C. Deformation substructures and fault configurations were investigated via TEM. After straining for ~2% (Figs. 8(a-b)), matrix dislocations were found to be strongly curved and deposited at the matrix/precipitate interfaces, implying the ordered $L1_2$ precipitates possess a strong deformation resistance towards matrix dislocation shearing. We also

occasionally observed particle shearing events that involved antiphase boundary (yellow arrow) and stacking fault (white arrow) formation (shown in Fig. 8(a)). It should be noted that, to lower the gliding resistance, pairwise dislocation movement is needed to deform the ordered L1$_2$ structure, that is, pairs of the 1/2<110> dislocations jointly shear the particles, limiting an antiphase boundary (APB) in between to minimize the energy. Therefore, antiphase-boundary-coupled dislocation pairs are involved in the APB-type particle shearing. The density of particle shearing via stacking fault further increased as the plastic strain increased to ~15% (as pointed out by white arrows in Fig. 8(c)). A close-up view of the fault region via high-resolution TEM indicated that the prefect "ABCABCABC" stacking sequence was disrupted into the "ABCBCABCA" stacking sequence. Therefore, the type of stacking fault can be determined as superlattice intrinsic stacking fault (SISF). As determined from Burgers circuit analyses (in the inset of Fig. 8(d)), this type of fault configuration formed in the wake of a partial dislocation with a Burgers vector of $\mathbf{b} = 1/3$ $[2\bar{}1\bar{}1]$ shearing into the L1$_2$ particles. According to Kear et al. [51,52], dislocation reactions at the matrix/particle interface lead to the formation of the SISF:(2)12[1$\bar{}$01]+12[1$\bar{}$1$\bar{}$0]→13[2$\bar{}$1$\bar{}$1]+16[2$\bar{}$1$\bar{}$1]

The dislocation with a Burgers vector of 13[2$\bar{}$1$\bar{}$1] enters the ordered L1$_2$ precipitates, leaving the SISF behind, while the 16[2$\bar{}$1$\bar{}$1] dislocation is left at the interface. Such particle shearing events, which involved the reaction of two dissociated Shockey partial dislocations at the interface and the gliding of dislocations into the particles, can be thermally activated in the PH-HEAs at 775 °C. A similar SISF particle shearing configuration has also been reported in Co–Al–W-based superalloys after deformation at elevated temperatures [53]. Apart from particle shearing via SISF and APB, plastic deformation also proceeded via bowing of the dislocations around the ordered precipitates (blue arrow in Fig. 8(c)). The applied stress drives dislocations moving forward and left loops around the L1$_2$ particles with the gliding of dislocations.

To summarize, the tensile deformation of the PH-HEAs encountered severe embrittlement in the intermediate temperature regime with a distinct transgranular-to-intergranular fracture mode transition. Profound GND pile-ups were found along grain boundaries to accommodate thermally activated grain boundary sliding (Figs. 9(a-b)). Intergranular voids nucleate at grain boundaries with accumulated GNDs, and coalesce into microcracks with the proceeding of tensile formation, which eventually lead to the tensile failure (Figs. 9(a-b)). Environmentally assisted grain boundary damage further intensified the embrittlement by oxygen penetration preferentially along intergranular paths, leading to a local grain boundary decohesion (Fig. 9(c)). To protect the PH-HEA specimens from the environmental embrittlement and reveal the intrinsic mechanical properties, we conducted the tensile test in an inert testing atmosphere and found a substantial tensile ductility recovery from 3.8 ± 0.3% in the oxidizing laboratory air to 15.0 ± 0.2% in a protective argon atmosphere at 775 °C. Instead of the intrinsic mechanical properties degradation, the tensile ductility drop at the intermediate temperature regime should mainly be ascribed to the environmentally assisted grain boundary attack. The intrinsic deformation substructures and dislocation-precipitation interactions were carefully checked after the tensile deformation in a protective argon

atmosphere at 775 °C (Fig. 9(d)). Matrix dislocations were found to be strongly curved and bow around the $L1_2$ precipitates. With the proceeding of the plastic deformation, external stress drove dislocations moving forward and left dislocation loops around the $L1_2$ particles. Besides dislocation looping, two types of particle shearing events were also discovered, namely the APB-coupled dislocation pair shearing and SISF-type shearing.
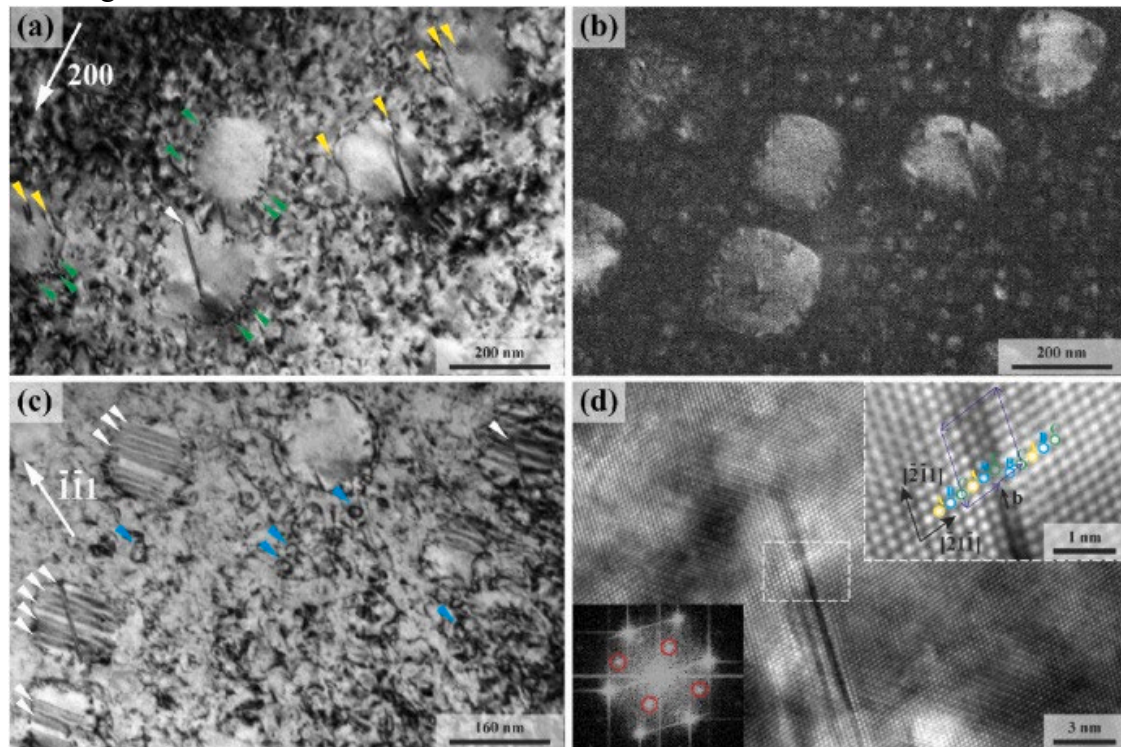

Fig. 8. Deformation substructures of the PH-HEA after ~2% plastic deformation at 775 °C in an inert argon atmosphere: (a) bright-field and (b) dark-field TEM micrographs showing particle shearing via stacking fault (white arrow) and antiphase boundary (yellow arrow). Dislocations bowing around the precipitates are pointed out by green arrows. $\mathbf{B} = [011]$. (c) Increased density of stacking fault shearing events as the plastic strain increased to ~15%. Dislocation looping around particles can also be observed at this strain level (blue arrow). $\mathbf{B} = [011]$. (d) High-resolution TEM image gave a closer view of the stacking fault structure in the $L1_2$ precipitates. Stacking sequence at the faulted region is highlighted in the inset, indicating the formation of superlattice intrinsic stacking fault in the $L1_2$ particle after dislocation shearing.
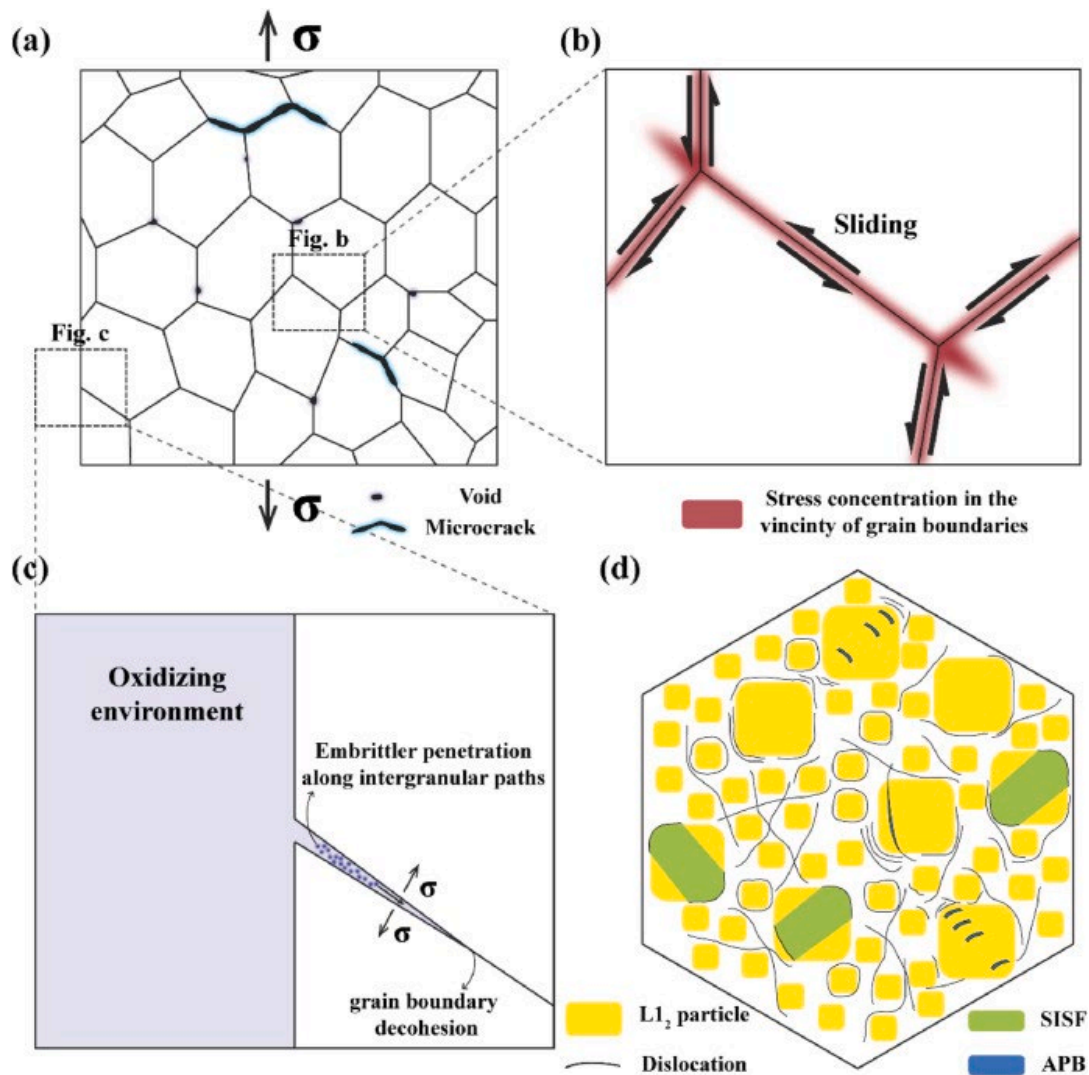
1. Download : Download high-res image (811KB)

   Fig. 9. Schematic illustrations of the deformation behavior of the polycrystalline PH-HEAs in the intermediate temperature regime. (Abbreviations: SISF, superlattice intrinsic stacking fault; APB, antiphase boundary).

5. Conclusions

In this study, we systematically investigated the temperature-dependent tensile properties and deformation mechanisms of a precipitation-hardened high-entropy alloy. The present findings can be summarized by the following points:

1) The duplex-aging heat treatment induced the formation of high-density $L1_2$ precipitates with bimodal size distribution within the FCC matrix. APT analyses indicated that Ni, Al, and Ti were potent $L1_2$-stabilizing elements by strongly partitioning to the precipitates, whereas Co, Fe, and Cr acted as the $L1_2$-destabilizing elements and were partitioning to the matrix.

2) The PH-HEAs demonstrated a decent tensile ductility at temperatures below 600 °C. The PH-HEA specimens fractured in a ductile dimpled transgranular mode with the tensile elongations over 20% within this temperature regime. A sudden drop in the

tensile ductility was found in the intermediate temperature regime, reaching the minimum with a fracture elongation of only 3.8% at 775 °C. Fractographical investigations revealed a distinct transgranular-to-intergranular fracture mode transition with the increased deformation temperature. Pronounced GNDs accumulated in the vicinity of grain boundaries to accommodate the thermally activated grain boundary sliding. Grain boundaries with severe stress concentration served as preferential sites for the void and crack initiation. Growth and linkage of the microcracks led to the destructive tensile failure.

3) In contrast with the rapid tensile fracture in the laboratory air, thermal barrier coating and protective testing atmosphere helped to recover the tensile ductility to $7.4 \pm 1.0\%$ and $15.0 \pm 0.2\%$ at 775 °C, respectively. Therefore, the tensile ductility drop in the intermediate temperature regime should be mainly ascribed to the environmental damage in the oxidizing atmosphere. The penetrating oxygen led to the grain boundary cohesion loss at the crack tip, allowing for the crack tip to advance aided by a local stress and shift the crack tip and the embrittling species inwards. This process facilitated intergranular crack propagation, resulting in a premature tensile failure.

4) The deformation substructures at 775 °C in a protective atmosphere revealed various types of dislocation-precipitation interactions. Dislocations bowed around and bypassed the $L1_2$ particles via the Orowan looping mechanism. Besides, two types of particle shearing mechanisms were also active, namely the APB-coupled dislocation pair shearing and the SISF-type shearing.

Declaration of competing interest

The authors declare that they have no known competing financial interests or personal relationships that could have appeared to influence the work reported in this paper.

References

[1] E.P. George, D. Raabe, R.O. Ritchie, High-entropy alloys, Nat. Rev. Mater. 4 (2019) 515e534.

[2] C. Lee, Y. Chou, G. Kim, M.C. Gao, K. An, J. Brechtl, C. Zhang, W. Chen, J.D. Poplawsky, G. Song, Lattice-distortion-enhanced yield strength in a refractory high-entropy alloy, Adv. Mater. 32 (2020) 2004029.

[3] Z. Wang, C. Wang, Y.-L. Zhao, Y.-C. Hsu, C.-L. Li, J.-J. Kai, C.-T. Liu, C.-H.

Hsueh, High hardness and fatigue resistance of CoCrFeMnNi high entropy alloy films with ultrahigh-density nanotwins, Int. J. Plast. 131 (2020) 102726.

[4] Y. Zhang, T.T. Zuo, Z. Tang, M.C. Gao, K.A. Dahmen, P.K. Liaw, Z.P. Lu, Microstructures and properties of high-entropy alloys, Prog. Mater. Sci. 61 (2014) 1e93.

[5] T. Yang, Y. Zhao, Y. Tong, Z. Jiao, J. Wei, J. Cai, X. Han, D. Chen, A. Hu, J. Kai, C.T. Liu, Multicomponent intermetallic nanoparticles and superb mechanical behaviors of complex alloys, Science 362 (2018) 933e937.

[6] Y. Zhao, Y. Li, G. Yeli, J. Luan, S. Liu, W. Lin, D. Chen, X. Liu, J. Kai, C.T. Liu, Anomalous precipitate-size-dependent ductility in multicomponent highentropy alloys with dense nanoscale precipitates, Acta Mater. (2021) 117480.

[7] T. Yang, Y. Zhao, J. Luan, B. Han, J. Wei, J. Kai, C.T. Liu, Nanoparticlesstrengthened high-entropy alloys for cryogenic applications showing an exceptional strength-ductility synergy, Scripta Mater. 164 (2019) 30e35.

[8] Y. Zhao, T. Yang, B. Han, J. Luan, D. Chen, W. Kai, C.T. Liu, J.-j. Kai, Exceptional nanostructure stability and its origins in the CoCrNi-based precipitationstrengthened medium-entropy alloy, Mater. Res. Lett. 7 (2019) 152e158.

[9] B. Cao, T. Yang, W.H. Liu, C.T. Liu, Precipitation-hardened high-entropy alloys for high-temperature applications: a critical review, MRS Bull. 44 (2019) 854e859.

[10] Y.-T. Chen, Y.-J. Chang, H. Murakami, T. Sasaki, K. Hono, C.-W. Li, K. Kakehi, J.W. Yeh, A.-C. Yeh, Hierarchical microstructure strengthening in a single crystal high entropy superalloy, Sci. Rep. 10 (2020) 1e11.

[11] K.-Y. Tsai, M.-H. Tsai, J.-W. Yeh, Sluggish diffusion in Co-Cr-Fe-Mn-Ni highentropy alloys, Acta Mater. 61 (2013) 4887e4897.

[12] B. Cao, Y. Zhao, T. Yang, C.T. Liu, L12-Strengthened Co-rich alloys for hightemperature structural applications: a critical review, Adv. Eng. Mater. 23 (2021) 2100453.

[13] B. Cao, H. Kong, Z. Ding, S. Wu, J. Luan, Z. Jiao, J. Lu, C.T. Liu, T. Yang, A novel L12-strengthened multicomponent Co-rich high-entropy alloy with both high g0-solvus temperature and superior high-temperature strength, Scripta Mater. 199 (2021) 113826.

[14] T. Watanabe, S. Tsurekawa, The control of brittleness and development of desirable mechanical properties in polycrystalline systems by grain boundary engineering, Acta Mater. 47 (1999) 4171e4185.

[15] N. Hansen, HallePetch relation and boundary strengthening, Scripta Mater. 51 (2004) 801e806.

[16] E. Lehockey, G. Palumbo, On the creep behaviour of grain boundary engineered nickel 1, Mater. Sci. Eng. 237 (1997) 168e172.

[17] R. Raj, M. Ashby, Intergranular fracture at elevated temperature, Acta Metall. Mater. 23 (1975) 653e666.

[18] A. Pineau, A.A. Benzerga, T. Pardoen, Failure of metals I: brittle and ductile fracture, Acta Mater. 107 (2016) 424e483.

[19] A. Devaraj, L. Kovarik, E. Kautz, B. Arey, S. Jana, C. Lavender, V. Joshi, Grain boundary engineering to control the discontinuous precipitation in multicomponent

U10Mo alloy, Acta Mater. 151 (2018) 181e190.

[20]K. Ming, L. Li, Z. Li, X. Bi, J. Wang, Grain boundary decohesion by nanoclustering Ni and Cr separately in CrMnFeCoNi high-entropy alloys, Sci. Adv. 5 (2019): eaay0639.

[21]T. Yang, Y. Zhao, W. Li, C. Yu, J. Luan, D. Lin, L. Fan, Z. Jiao, W. Liu, X. Liu, C.T. Liu, Ultrahigh-strength and ductile superlattice alloys with nanoscale disordered interfaces, Science 369 (2020) 427e432.

[22]T. Yang, Y. Zhao, L. Fan, J. Wei, J. Luan, W. Liu, C. Wang, Z. Jiao, J. Kai, C.T. Liu, Control of nanoscale precipitation and elimination of intermediatetemperature embrittlement in multicomponent high-entropy alloys, Acta Mater. 189 (2020) 47e59.

[23]B. Cao, H. Kong, L. Fan, J. Luan, Z. Jiao, J. Kai, T. Yang, C.T. Liu, Heterogenous columnar-grained high-entropy alloys produce exceptional resistance to intermediate-temperature intergranular embrittlement, Scripta Mater. 194 (2021) 113622.

[24]S. Wu, G. Wang, Q. Wang, Y. Jia, J. Yi, Q. Zhai, J. Liu, B. Sun, H. Chu, J. Shen, Enhancement of strength-ductility trade-off in a high-entropy alloy through a heterogeneous structure, Acta Mater. 165 (2019) 444e458.

[25]L. Zheng, G. Schmitz, Y. Meng, R. Chellali, R. Schlesiger, Mechanism of intermediate temperature embrittlement of Ni and Ni-based superalloys, Crit. Rev. Solid State Mater. Sci. 37 (2012) 181e214.

[26]S. Xie, S. Lin, Q. Shi, W. Wang, C. Song, W. Xu, M. Dai, A study on the mechanical and thermal shock properties of MCrAlY coating prepared by arc ion plating, Surf. Coating. Technol. 413 (2021) 127092.

[27]A.J. Wilkinson, D. Randman, Determination of elastic strain fields and geometrically necessary dislocation distributions near nanoindents using electron back scatter diffraction, Philos. Mag. A 90 (2010) 1159e1177.

[28]R. Mulford, U. Kocks, New observations on the mechanisms of dynamic strain aging and of jerky flow, Acta Metall. Mater. 27 (1979) 1125e1134.

[29]J. Robinson, M. Shaw, Microstructural and mechanical influences on dynamic strain aging phenomena, Int. Mater. Rev. 39 (1994) 113e122.

[30]D.R. Clarke, S.R. Phillpot, Thermal barrier coating materials, Mater. Today 8 (2005) 22e29.

[31]J. Cai, S. Yang, L. Ji, Q. Guan, Z. Wang, Z. Han, Surface microstructure and high temperature oxidation resistance of thermal sprayed CoCrAlY coating irradiated by high current pulsed electron beam, Surf. Coating. Technol. 251 (2014) 217e225.

[32]S. Bose, J. DeMasi-Marcin, Thermal barrier coating experience in gas turbine engines at Pratt & Whitney, J. Therm. Spray Technol. 6 (1997) 99e104.

[33]M. Carroll, L. Carroll, Developing dislocation subgrain structures and cyclic softening during high-temperature creepefatigue of a nickel alloy, Metall. Mater. Trans. 44 (2013) 3592e3607.

[34]J.L. Carter, M.W. Kuper, M.D. Uchic, M.J. Mills, Characterization of localized deformation near grain boundaries of superalloy Rene-104 at elevated temperature, Mater. Sci. Eng. 605 (2014) 127e136.

[35]J. Xu, H. Gruber, D. Deng, R.L. Peng, J.J. Moverare, Short-term creep behavior of an additive manufactured non-weldable Nickel-base superalloy evaluated by slow

strain rate testing, Acta Mater. 179 (2019) 142e157.

[36] P. Kontis, E. Alabort, D. Barba, D.M. Collins, A.J. Wilkinson, R.C. Reed, On the role of boron on improving ductility in a new polycrystalline superalloy, Acta Mater. 124 (2017) 489e500.

[37] L. Wang, J. Zhou, S. Zhang, Y. Liu, S. Dong, Effects of accommodated grain boundary sliding on triple junction nanovoid nucleation in nanocrystalline materials, Mech. Mater. 71 (2014) 10e20.

[38] D.A. Woodford, Gas phase embrittlement and time dependent cracking of nickel based superalloys, Energy Mater. 1 (2006) 59e79.

[39] J. Pfaendtner, C. McMahon Jr., Oxygen-induced intergranular cracking of a Nibase alloy at elevated temperaturesdan example of dynamic embrittlement, Acta Mater. 49 (2001) 3369e3377.

[40] L. Viskari, M. Ho€rnqvist, K. Moore, Y. Cao, K. Stiller, Intergranular crack tip oxidation in a Ni-base superalloy, Acta Mater. 61 (2013) 3630e3639.

[41] K. Sadananda, A. Vasudevan, Review of environmentally assisted cracking, Metall. Mater. Trans. 42 (2011) 279e295.

[42] R. Jiang, D. Proprentner, M. Callisti, B. Shollock, X. Hu, Y. Song, P. Reed, Role of oxygen in enhanced fatigue cracking in a PM Ni-based superalloy: stress assisted grain boundary oxidation or dynamic embrittlement? Corrosion Sci. 139 (2018) 141e154.

[43] V. Paidar, D. Pope, V. Vitek, A theory of the anomalous yield behavior in L12 ordered alloys, Acta Metall. Mater. 32 (1984) 435e448.

[44] D. Bika, C. McMahon Jr., A model for dynamic embrittlement, Acta Metall. Mater. 43 (1995) 1909e1916.

[45] P. Gordon, H.H. An, The mechanisms of crack initiation and crack propagation in metal-induced embrittlement of metals, Metall. Trans. A 13 (1982) 457e472.

[46] L. Xu, Y. Cheng, Corrosion of X100 pipeline steel under plastic strain in a neutral pH bicarbonate solution, Corrosion Sci. 64 (2012) 145e152.

[47] M. Zhou, W. Yao, X. Yang, Z. Peng, K. Li, C. Dai, W. Mao, Y. Zhou, C. Lu, In-situ and real-time tests on the damage evolution and fracture of thermal barrier coatings under tension: a coupled acoustic emission and digital image correlation method, Surf. Coating. Technol. 240 (2014) 40e47.

[48] W. Yao, C. Dai, W. Mao, C. Lu, L. Yang, Y. Zhou, Acoustic emission analysis on tensile failure of air plasma-sprayed thermal barrier coatings, Surf. Coating. Technol. 206 (2012) 3803e3807.

[49] R. Maldonado, E. Nembach, The formation of precipitate free zones and the growth of grain boundary carbides in the nickel-base superalloy NIMONIC PE16, Acta Mater. 45 (1997) 213e224.

[50] A.K. Vasudevan, R. Doherty, Grain boundary ductile fracture in precipitation hardened aluminum alloys, Acta Metall. Mater. 35 (1987) 1193e1219.

[51] B. Kear, A. Giamei, G. Leverant, J. Oblak, On intrinsic/extrinsic stacking fault pairs in the Ll2 lattice, Scripta Metall. Mater. 3 (1969) 123e129.

[52] B.H. Kear, J.M. Oblak, A.F. Giamei, Stacking faults in gamma prime Ni3(Al, Ti) precipitation hardened nickel-base alloys, Metall. Trans. A 1 (1970) 2477e2486.

[53] A. Suzuki, T.M. Pollock, High-temperature strength and deformation of g/g0 two-phase CoeAleW-base alloys, Acta Mater. 56 (2008) 1288e1297.